



Cite this: *J. Mater. Chem. A*, 2018, 6, 19853

Cobalt nickel nitride coated by a thin carbon layer anchoring on nitrogen-doped carbon nanotube anodes for high-performance lithium-ion batteries†

Rujia Zou, ^a Mingdong Xu, ^a Shu-Ang He, ^a Xiaoyu Han, ^b Runjia Lin, ^b Zhe Cui, ^a Guanjie He, ^{*bc} Daniel J. L. Brett, ^c Zheng Xiao Guo, ^b Junqing Hu, ^a and Ivan P. Parkin ^{*b}

Cobalt nickel nitrides coated by a thin carbon layer anchoring on nitrogen-doped carbon nanotubes, named $\text{NiCo}_2\text{N}@\text{C-NCNT}$ nanocomposites, were obtained by a facile fabrication method. The work reveals that the NiCo_2N structures possess extensive Li^+ channels and high electrical conductivity for the rapid electron/ion transfer in lithium-ion batteries (LIBs). These materials were applied as anodes for the first time, and a nanobattery was constructed and examined using a transmission electron microscope (TEM) to directly verify the *in situ* structural evolution during lithiation/delithiation processes. The results show a small dimensional expansion of the $\text{NiCo}_2\text{N}@\text{C-NCNT}$ nanocomposites during the lithiation process; this is due to the disciform expansion of the lithiated NiCo_2N nanoparticles which cover the surface of the NCNTs. It was found that some of the lithiated NiCo_2N nanoparticles moved along the surface of the NCNTs and entered the NCNTs – thus acting to ‘protect’ themselves. Moreover, electrodes composed of interconnected NCNTs alleviate the volumetric expansion of $\text{NiCo}_2\text{N}@\text{C-NCNT}$ nanocomposites. The $\text{NiCo}_2\text{N}@\text{C-NCNT}$ nanocomposite electrode exhibits excellent lithium storage properties in electrochemical tests in coin cell configurations. This material synthesis route and ‘self-protection’ mechanism provide the basis of a design strategy for developing effective electrode materials in LIBs and a broader sphere of metal-ion batteries.

Received 3rd September 2018
Accepted 19th September 2018

DOI: 10.1039/c8ta08537d
rsc.li/materials-a

Introduction

Rechargeable lithium-ion batteries (LIBs) are highly attractive for a wide range of applications. They have intrinsic advantages over many other battery types, including high energy density, long life-span, no memory effect and relatively low environmental impact.^{1–3} However, the increasing employment of LIBs and more stringent performance requirements in portable electronic devices, electric vehicles and hybrid electrical systems demand further improvements of the energy density, durability, rate capability and safety. The current progress relies to a large extent on the discovery of novel

materials and structural engineering of the electrodes.^{4–6} Recently, considerable efforts have been made to develop high-performance anode materials (*i.e.* high capacity with stability) using innovative materials and configurations.^{7–10} These two approaches exhibited notable advantages and disadvantages. Among electrode materials studied thus far, metal oxides,^{11,12} sulfides^{6,9} and alloys^{1,10} have been synthesized and outperformed commercial graphite anodes. However, these electrode materials generally have poor electrical conductivity, large volume changes and single reaction mechanism during the lithiation/delithiation process, which cannot satisfy the fast electron transport and stability requirements for high-performance LIBs.^{1–3} A typical approach to electrode design is to form a composite of these active materials with carbon to achieve core–shell, yolk–shell, arrays, porous nanostructures, *etc.*^{13,14} The topography of such electrode materials can tolerate large volume changes and cut down transport paths for both electrons and ions during the charge/discharge process. However, it is difficult for the as-mentioned structures to be obtained by facile, cost-effective and scalable techniques. Therefore, it remains a challenge to explore highly effective materials and structures for LIBs.

^aState Key Laboratory for Modification of Chemical Fibers and Polymer Materials, College of Materials Science and Engineering, Donghua University, Shanghai 201620, China

^bChristopher Ingold Laboratory, Department of Chemistry, University College London, 20 Gordon Street, London WC1H 0AJ, UK. E-mail: guanjie.he.14@ucl.ac.uk; *i.p.parkin@ucl.ac.uk*

^cElectrochemical Innovation Lab, Department of Chemical Engineering, University College London, London WC1E 7JE, UK

† Electronic supplementary information (ESI) available. See DOI: [10.1039/c8ta08537d](https://doi.org/10.1039/c8ta08537d)

Metal nitrides (MNs) have attracted enormous research attention due to their electrochemical activity and metallic conductivity. It has been confirmed that the introduction of N atoms strongly affects the electronic structure of the metal hosts by charge-transfer and/or concomitant structural modification.^{15,16} Various MN nanostructures, including nanoparticles,¹⁷ nanosheets,¹⁸ nanocubes¹⁹ and nanowires,²⁰ have been designed and demonstrated as potential electrodes for LIBs. Moreover, it is worth noting that highly efficient electrochemical energy storage performance of such materials can be achieved through the use of tailored nanostructures with optimized electrical conductivity, active sites, and sufficient inter-space for alleviating the volume changes that occur in ion intercalation/deintercalation.¹⁵ Recently, cobalt nickel nitrides have been demonstrated as outstanding candidates for energy storage and conversion applications, such as electrocatalysts in the hydrogen and oxygen evolution reactions,^{21,22} due to their high electrical conductivity and optimized reactive sites compared to conventional metal oxide counterparts. However, studies on utilization, structural design and understanding of the mechanism of these metal nitrides in LIBs are seldom reported.

In this work, the synthesis of cobalt nickel nitride coated by a thin carbon layer anchored on nitrogen-doped carbon nanotubes (NCNTs), *i.e.* NiCo₂N@C-NCNT nanocomposites, by a simplified process and their anode application in LIBs are reported for the first time. NCNT based composites exhibited excellent Li storage capability due to their large surface area, high electrical conductivity, excellent thermal and chemical stability, and relatively low volume expansion/contraction due to self-supported frameworks. This work reveals that the NiCo₂N electrode materials possess multiple channels for the diffusion of Li⁺ ions and higher electrical conductivity for fast electron/ion transfer in comparison with the commonly used conversion-type analogs, such as NiCo₂O₄ materials. *In situ* transmission electron microscopy (TEM) observations verify a small dimensional expansion of NiCo₂N@C-NCNT nanocomposites during the lithiation process due to the disciform expansion of lithiated NiCo₂N nanoparticles covering the surface of NCNTs. Notably, some of the lithiated NiCo₂N nanoparticles spread along the surface of NCNTs, and enter the NCNTs to 'protect themselves', which leads to the excellent cycling stability of these integrated structures. In addition, an electrode composed of interconnected NiCo₂N@C-NCNTs could alleviate the total volumetric expansion during the lithiation/delithiation process. The NiCo₂N@C-NCNT nanocomposite electrode exhibits high specific capacity (\sim 624.5 mA h g⁻¹ at a current density of 2000 mA g⁻¹), excellent cycling stability (retention close to 104.5% after 300 cycles) and high rate capability, suggesting that it is a desirable anode material for high-performance LIBs.

Materials and methods

Simulation methods

On-site Hubbard corrected Density Functional Theory (DFT+U) calculations were carried out using the Vienna ab initio Package

(VASP).^{23,24} The Perdew–Burke–Ernzerhof (PBE) functional²⁵ for the exchange–correlation term was used with the projector augmented wave method.^{26,27} A plane wave cutoff of 500 eV with forces converged to 0.01 eV Å⁻¹. A gamma centred $5 \times 5 \times 5$ *K* point grid was used for the sampling. Dudarev's method was adopted for the setting of U_{eff}, where Ni and Co were set to 6.2 and 3.32 eV, respectively.²⁸ The Climbing image modified Nudged Elastic Band (Ci-NEB) method was employed to study the Li atom diffusion behavior.^{29,30}

Synthesis. All chemicals used in this work are commercially available from Sigma-Aldrich and were used as received without further purification. The NiCo₂N@C-NCNT nanocomposites were synthesized using a hydrothermal reaction combined with a simple thermal treatment under NH₃. In a typical synthesis, 12 mg of the mildly oxidized CNTs were dissolved in 35 mL of ethanol by ultrasonication for 1 h. Then, 2.5 mL of 0.2 M Co(NO₃)₂·6H₂O methanol solution and 2.5 mL of 0.1 M Ni(NO₃)₂·6H₂O methanol solution were added to the CNT ethanol solutions with magnetic stirring for 10 min. This was followed by the addition of 0.225 g of methenamine with further stirring for 30 min to prepare the precursor solution with a Co : Ni atomic ratio of 2 : 1. The as-prepared solution was kept at 80 °C for 10 h. After that, the solution was transferred to 50 mL autoclaves and kept at 160 °C for 10 h. The resulting product was collected by centrifugation and washed with ethanol and water in sequence and lyophilized. NiCo₂N@C-NCNT nanocomposites were prepared by annealing the hydroxides/CNT hybrids under a 200-standard cubic centimeter per minutes (sccm) flow of ammonia gas flow with a temperature rate of 5 °C min⁻¹ up to 580 °C for 3 h. NiCo₂O₄-CNT nanocomposites were synthesized by annealing the as-prepared hydroxide materials under air flow at 350 °C for 2 h with the same flow and temperature rates.

Characterization. The sample morphology and microstructure were characterized by TEM (JEM-2100F equipped with an energy-dispersive X-ray spectrometer). The X-ray diffraction (XRD) patterns were recorded using a STOE SEIFERT X-ray diffractometer with Mo K α radiation and a Philips X' Pert MRD with Cu K α radiation. The surface chemical information was characterized by X-ray photoelectron spectroscopy (XPS) using a Thermo Scientific K-alpha photoelectron spectrometer. The *in situ* TEM observation of the lithiation/delithiation processes was carried out using a scanning tunneling microscopy (STM)-TEM holder commercially available from Nanofactory Instruments AB in JEOL 2100F TEM operated at 200 kV.

Electrochemical measurements. The working electrodes were prepared by mixing the active materials (NiCo₂N@C-NCNT nanocomposites or NiCo₂O₄-CNT nanocomposites), conductive agent (carbon black) and binder (sodium alginate) in a weight ratio of 70 : 20 : 10. The typical loading density of active materials of the NiCo₂N@C-NCNT nanocomposite was \sim 1.2 mg cm⁻². Coin-type cells (CR2032) were fabricated using lithium metal as the counter electrode, Celgard 2400 (Charlotte, NC, USA) as the separator and LiPF₆ (1 M) in ethylene carbonate–dimethyl carbonate (1 : 1 vol%) as the electrolyte in an argon-filled glove box (with both the moisture and the oxygen concentration below 1 ppm). The galvanostatic measurements



were carried out on a LAND-CT2001A battery tester with a voltage window of 0.01–3.0 V at various current rates. CV measurements at 0.1 mV s^{−1} over the range of 0.01–3.0 V (vs. Li/Li⁺) and electrochemical impedance spectra in the frequency range of 100 kHz to 0.01 Hz were conducted on an Autolab (PGSTAT302N) electrochemical workstation.

Results and discussion

The diffusivity of Li⁺ ions in bulk NiCo₂N was studied and compared with NiCo₂O₄ by density functional theory.^{23,24} The NiCo₂N crystal was derived from the same structure of Ni₃N (*P*6₃22). The lattice parameters were optimized by the energy-volume minimum (at constant *c/a* ratio), and the estimated values were *a* = 4.584 Å and *c* = 4.272 Å. Two possible Ni/Co arrangements were considered and are shown in Fig. S1.[†] The one showing Ni atoms close to each other (Fig. S1a[†]) has 5.62 meV per atom lower formation energy compared to the other one (Fig. S1b[†]). Hence, a further study on the Li-ion diffusion was adopted in the Ni nearby arrangement, with a 2 × 2 × 2 supercell. As shown in Fig. 1 and S2–S4,[†] there are three proposed tunnels for Li⁺ ions to diffuse through the bulk materials, one along the [001] direction and two along the [100] direction, denoted as path A, B and C, respectively. For all three pathways, the calculated energy barriers using the Ci-NEB method are shown in Fig. 1c and S2–S4.[†] Path A possesses the lowest energy barrier of 0.396 eV. However, path B and C are energetically greater by 76 and 96 meV. The Li⁺ ions diffusion for NiCo₂O₄ was analyzed by the same method, whereas no possible intercalation tunnels for Li⁺ ions could be detected to diffuse through the bulk materials of NiCo₂O₄ due to the geometry limitation. The computational analysis shows that the NiCo₂N electrode materials deliver multiple channels for the diffusion of Li⁺ ions. The multiple channels for the diffusion of Li⁺ ions and high electrical conductivity for the fast electron/ion transfer play a significant role for anode materials in high-performance LIBs. To synthesize and utilize NiCo₂N materials

as anodes in LIBs, a straight-forward procedure for the composites of carbon coated NiCo₂N on NCNT nanostructures was exploited and is shown in Fig. 1d. In brief, NiCo₂N@C-NCNT nanocomposites were obtained *via* a combined hydrolysis, solvothermal synthesis and annealing process. Firstly, the oxidized multi-walled CNTs were dispersed into an alcoholic solution containing Ni²⁺ and Co²⁺. The NiCo precursors were grown uniformly on the surface of oxidized CNTs after hydrolysis. In the second step, the NiCo precursors on the surface of oxidized CNTs were converted to NiCo hydroxide nanosheets (Fig. S5[†]). The final ammonization process induced the formation of NiCo₂N@C-NCNT nanocomposites.

The morphology and structure of the as-prepared NiCo₂N@C-NCNT composite were uncovered by TEM and high-resolution TEM (HRTEM) images, as shown in Fig. 2. As shown in Fig. 2a and S6,[†] NiCo₂N nanoparticles grew on the surface of NCNTs. The diameter of the NiCo₂N nanoparticles ranged from ~10 to ~20 nm. Close observation (Fig. 2b) revealed that the surface of NiCo₂N nanoparticles was covered with thin carbon layers, thus forming a NiCo₂N@C core-shell nanostructure. In addition, NiCo₂N@C nanoparticles were attached on NCNTs and constituted the NiCo₂N@C-NCNT composite, as shown in Fig. 2b. The HRTEM image shown in Fig. 2c demonstrates the crystalline features of NiCo₂N@C nanoparticles with a carbon layer on the NiCo₂N nanoparticles. Energy-dispersive X-ray spectroscopy (EDX) mappings clarified that Ni, Co, N and C uniformly exist in NiCo₂N@C-NCNT nanocomposites (Fig. 2d–h). The main elements, *i.e.* Co, Ni and N, are well-dispersed on the surface of the CNTs and overlapped with each other. In addition, as illustrated in Fig. 2g, N elements were evenly distributed on CNTs, which suggests the successful nitrogen doping on the CNTs. It is widely known that the N-doped CNTs can be favorable for electron transfer *via* contribution from lone electron pairs, preventing the formation of Li⁺ clusters, strengthening Li⁺ adsorption and increasing wettability.³¹ Furthermore, the presence of Ni, Co and N on the NCNTs showed an approximate

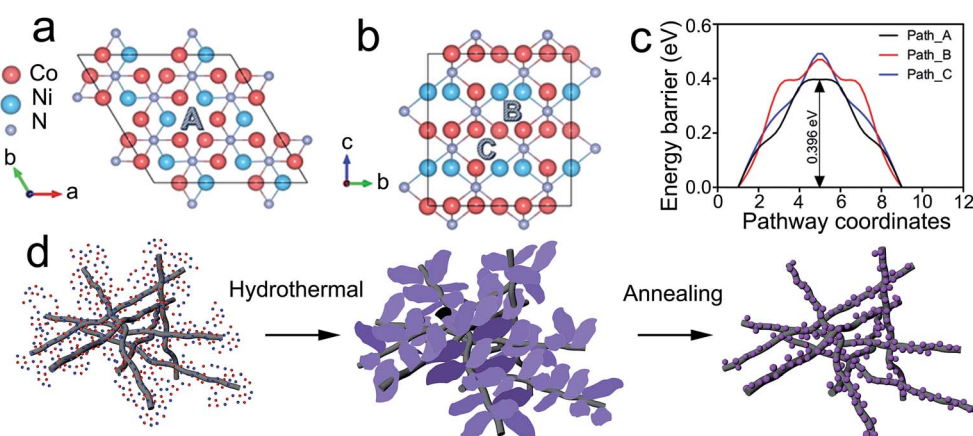


Fig. 1 (a and b) Three proposed Li diffusion tunnels, denoted as path A, path B and path C. A represents Li diffusion along the [001] direction. B and C represent Li diffusion along the [100] direction, with different neighbour Ni/Co arrangements. The red, blue and purple balls represent Co, Ni and N atoms, respectively. (c) The calculated energy barriers for the Li atom intercalated through pathways A, B and C. (d) Synthetic process of the NiCo₂N@C-NCNT nanocomposites.



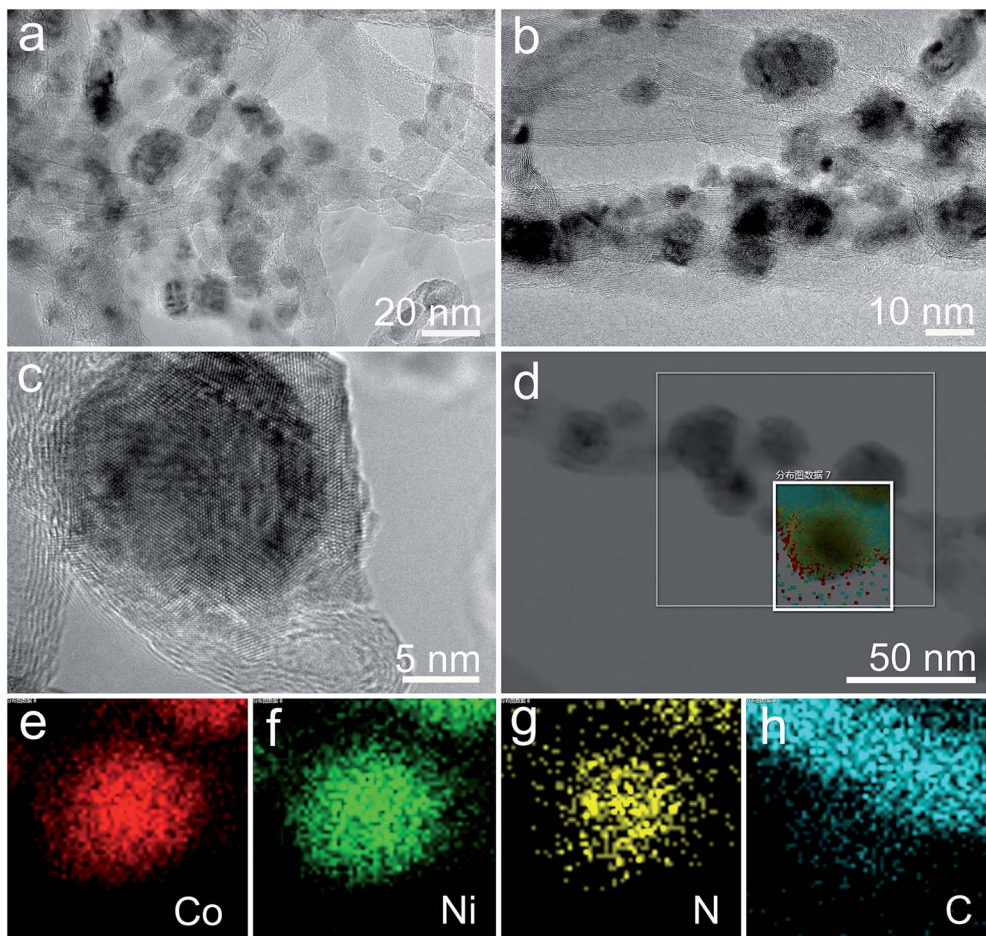


Fig. 2 (a and b) TEM images and (c) HRTEM image of NiCo_2N @C-NCNT nanocomposites. (d–h) EDX elemental mapping of NiCo_2N @C-NCNT nanocomposites (d), elements of Co (e), Ni (f), N (g), and C (h), respectively.

atomic ratio of 1.00 : 2.09 : 1.14 (NiCo_2N calculated for Ni, Co, N = 1.00 : 2.00 : 1.00). The relatively high proportion of the N atomic abundance in the spectra probably originated from the N-doped CNTs. The mapping images further clarified that the surface of the NiCo_2N nanoparticles was covered with a thin carbon layer, which is consistent with Fig. 2h and HRTEM observations (Fig. 2c). These thin carbon layers could provide clear superiorities for electrode materials in LIBs because of their excellent transport properties and better mechanical strength for both Li^+ ions and electrons among NiCo_2N nanoparticles, NCNTs and conductive agents.

To further investigate the chemical composition of the as-obtained NiCo_2N @C-NCNT nanocomposites, X-ray photoelectron spectroscopy (XPS) characterization was carried out. As illustrated in Fig. 3a, the peaks of the Ni 2p region at ~ 856.2 (Ni 2p_{3/2}) and 973.9 eV (Ni 2p_{1/2}), and a pair of satellite peaks ($\Delta\text{Ni} = 18.9$ eV) correspond to the hybrid valence states of +2 and +1 Ni at the material surface.³² The Co 2p region (Fig. 3b) exhibits two peaks at ~ 797.2 and 781.2 eV, identifying Co 2p_{1/2} and Co 2p_{3/2}, respectively, which are characteristics of Co^{2+} and Co^+ .³² The N 1s region (Fig. 3c) shows a strong peak at ~ 398.5 eV, which corresponds to metallic Ni/Co and nitrogen bonds indicative of N^{3-} species, indicating successful synthesis of the Ni–Co–N

composite.³³ In addition, the C 1s peak shows carbon–nitrogen bonds at ~ 285.6 eV, demonstrating the successfully N-doped CNTs.³⁴ The XPS survey spectrum of the NiCo_2N @C-NCNT nanocomposites in Fig. 3 confirms the existence of Ni, Co, N, and C elements. The atomic ratio of Ni to Co (Ni/Co) is about 1.00 : 2.16, suggesting the slightly Co-rich surfaces of the composite materials. Fig. S7† presents the X-ray diffraction (XRD) pattern of the NiCo_2N @C-NCNT nanocomposite. The diffraction peaks showed a shift compared to that of the standard hexagonal Ni_3N pattern ($P6_322$; JCPDS10-0280), indicating the formation of uniform bimetal nitride solid solutions. No other diffraction peaks were observed, demonstrating phase-pure metal nitrides at an annealing temperature of 580°C .

Electrochemical performance of the as-prepared NiCo_2N @C-NCNT nanocomposites is evaluated in coin-type half cells as an anode material for LIBs. Fig. 4a displays the cyclic voltammetry (CV) curves of NiCo_2N @C-NCNT nanocomposites for the 1st, 2nd, 5th and 10th cycles at a scan rate of 1 mV s^{-1} in the voltage window of 0.01 – 3 V *versus* Li/Li^+ . In the first cycle, irreversible reduction peaks of the NiCo_2N @C-NCNT nanocomposites at around 1.24 V can be noted, which could be assigned to the reduction of $\text{Ni}^{2+}/\text{Ni}^+$ and $\text{Co}^{2+}/\text{Co}^+$ to metallic Ni and Co.³⁵ The reduction peak at around 0.58 V was detected in

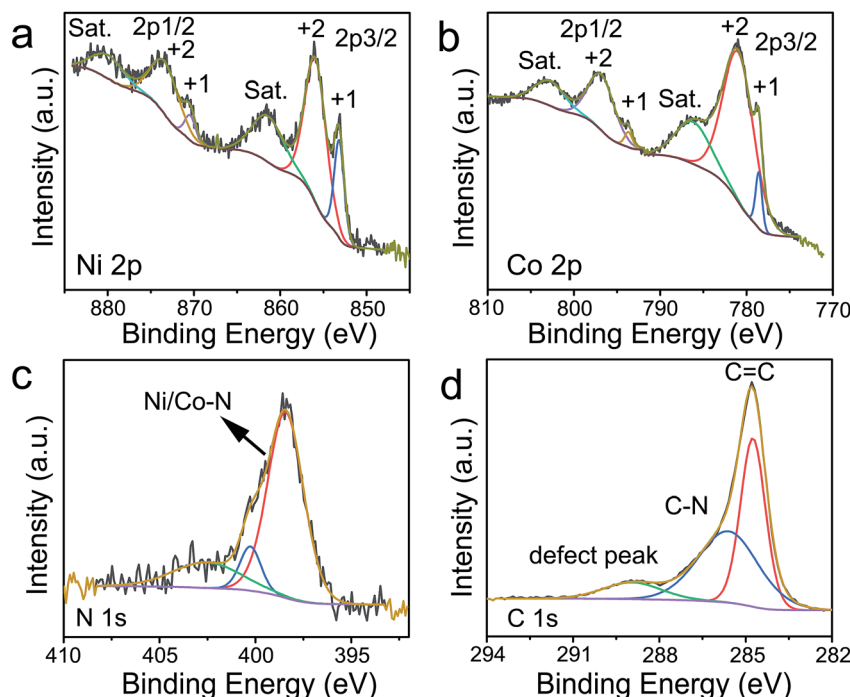


Fig. 3 XPS spectra of $\text{NiCo}_2\text{N}@\text{C-NCNT}$ nanocomposite structures: (a) Ni 2p, (b) Co 2p, (c) N 1s, and (d) C 1s.

the first cathodic scan, which can be ascribed to the formation of thin solid electrolyte interphase (SEI) layers resulting from the electrolyte reduction and deposition. Meanwhile, the anodic peaks of the $\text{NiCo}_2\text{N}@\text{C-NCNT}$ nanocomposites were at about 1.38 and 2.14 V and could be indexed to the oxidation of metallic Ni and Co to NiN_x and CoN_x , respectively. In the subsequent cycles, the overlapped CV curves of the 1st, 2nd, 5th and 10th cycles indicate good reversibility of the electrochemical reactions. The charge-discharge profiles of the $\text{NiCo}_2\text{N}@\text{C-NCNT}$ nanocomposite electrodes at a current density of 100 mA g^{-1} for the 1st, 2nd, and 3rd cycles are displayed in Fig. 4b. The distinct plateaus in the discharge and charge profiles are in accordance with the CV curves, matching well with the reduction and oxidation processes of NiN_x , CoN_x and metallic Ni, Co, respectively. The first cycle reveals discharge and charge capacities of 1077.2 and 725.2 mA h g^{-1} , respectively. The irreversible capacity loss for the first cycle should be attributed to the formation of a SEI, which has been commonly observed for NiCo_2O_4 and NiCo_2S_4 electrode materials.^{8,34} The discharge capacities of the electrode decreased to 739.8 and 718.2 mA h g^{-1} in the second and third cycles, respectively, and the corresponding coulombic efficiencies increased to $\sim 92.4\%$ and $\sim 94.5\%$. The sharply increased coulombic efficiency indicates that a stable SEI layer has already formed during the initial cycles.

The rate performance of the $\text{NiCo}_2\text{N}@\text{C-NCNT}$ nanocomposite electrode was evaluated at different current densities. As shown in Fig. 4c (dark yellow and magenta curves for the discharge and charge curves), the average discharge capacities of the $\text{NiCo}_2\text{N}@\text{C-NCNT}$ nanocomposites are ~ 726 to 747, 701, 652, 621 and 477 mA h g^{-1} at current densities of 100 to 200,

500, 1000, 2000 and 5000 mA g^{-1} , respectively. A higher capacity than graphite in LIBs can still be realized even at a high current rate of 5000 mA g^{-1} . Interestingly, at a high current density of 5000 mA g^{-1} , the discharge capacity of the $\text{NiCo}_2\text{N}@\text{C-NCNT}$ nanocomposites was $\sim 63\%$ of the initial value. When the current rate goes back to 100 mA g^{-1} , the $\text{NiCo}_2\text{N}@\text{C-NCNT}$ nanocomposites could quickly resume a reversible capacity of 756 mA h g^{-1} , corresponding to a capacity retention of $\sim 104.1\%$. Such a performance is impressive, indicating the excellent rate capability and reversibility of the electrode. For comparison, NiCo_2O_4 -CNT nanocomposites were synthesized (Fig. S8†) and their rate performance as the electrode was also tested and is shown in Fig. 4c (cyan and orange curves for the discharge and charge curves). The specific capacity of NiCo_2O_4 -CNT nanocomposite electrodes is much lower than that of the $\text{NiCo}_2\text{N}@\text{C-NCNT}$ nanocomposite electrode at the same current density, especially at high current densities. The capacities of the NiCo_2O_4 -CNT nanocomposite decreased from ~ 418 to 373, 301, 281, 237, 169 and 92 mA h g^{-1} when the current density was increased from 100 to 200, 500, 1000, 2000 and 5000 mA g^{-1} . Noticeably, the capacity of $\text{NiCo}_2\text{N}@\text{C-NCNT}$ nanocomposite electrode at a current density of 5000 mA g^{-1} is up to ~ 5 times higher than that of the NiCo_2O_4 -CNT nanocomposite electrode.

The cycling stability of $\text{NiCo}_2\text{N}@\text{C-NCNT}$ nanocomposite electrodes were further evaluated under both low and high current densities. As shown in Fig. 4d, $\text{NiCo}_2\text{N}@\text{C-NCNT}$ nanocomposites delivered a discharge capacity of ~ 718.3 mA h g^{-1} for the 4th cycle at the current density of 200 mA g^{-1} (the initial three cycles for the activation of $\text{NiCo}_2\text{N}@\text{C-NCNT}$ nanocomposites) and increased moderately to

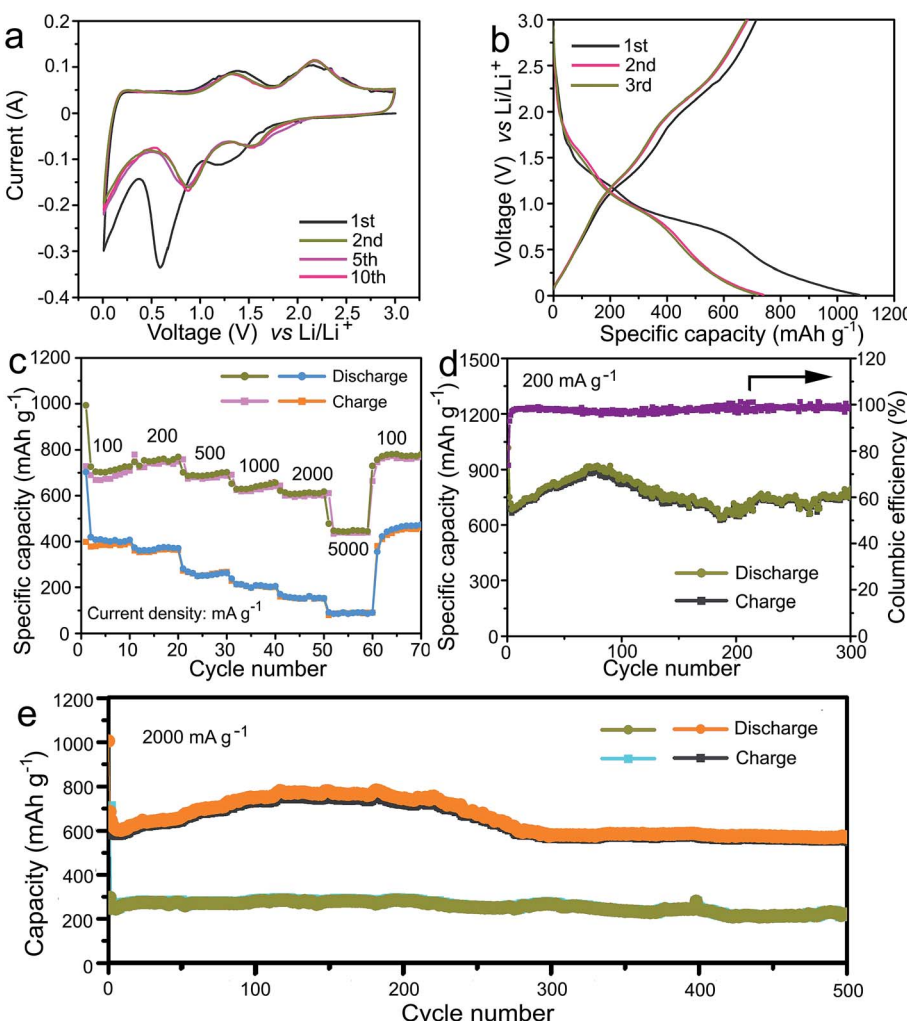


Fig. 4 (a) CV curves of NiCo₂N@C-NCNT nanocomposites at a scan rate of 0.1 mV s^{-1} between 0.01 and 3 V. (b) Charge-discharge curves of NiCo₂N@C-NCNT nanocomposites at a constant current density of 100 mA g^{-1} . (c) Rate performance of the NiCo₂N@C-NCNT nanocomposite at various current densities. (d) Cycling performance and corresponding coulombic efficiency of the NiCo₂N@C-NCNT nanocomposite measured at the current density of 200 mA g^{-1} . (e) Cycling performance of the NiCo₂N@C-NCNT nanocomposite and NiCo₂O₄-CNT nanocomposite measured at the high current density of 2000 mA g^{-1} .

$\sim 921.3 \text{ mA h g}^{-1}$ after the 79th cycle. Its specific capacity was gradually decreased to $\sim 721.8 \text{ mA h g}^{-1}$ after the 135th cycle, and then showed a steady trend and maintained at $\sim 750.6 \text{ mA h g}^{-1}$ for the 300th cycle. The capacity retention was 104.5% compared to the initial value, which shows apparent excellent cyclability. In addition, the columbic efficiency increased sharply from 73.8% for the first cycle to $>97\%$ after initial activation, and then stabilized there for up to 120 cycles. It is worth noting that the gradually increased performance after the initial cycles is mainly due to the special structural evolution of the NiCo₂N@C-NCNT nanocomposites *via* a 'self-protection' mechanism, which will be elaborated on the further discussion. Surprisingly, the NiCo₂N@C-NCNT nanocomposite electrodes still exhibited extremely good stability at a high current density of 2000 mA g^{-1} (Fig. 4e). The capacity was $\sim 624.5 \text{ mA h g}^{-1}$ in the 4th cycle at a current density of 2000 mA g^{-1} and remained at $\sim 569.1 \text{ mA h g}^{-1}$ after 500 cycles (orange and black curves for the discharge and charge

processes, respectively). The NiCo₂N@C-NCNT nanocomposite electrode showed a capacity fading rate of only 0.089% per cycle at a high current density, which is even smaller than those of previously reported nanostructured NiCo₂O₄, NiCo₂S₄ electrode materials or other electrode materials.^{8,35-39} For comparison, NiCo₂O₄-CNT nanocomposite as anodes were also evaluated at a high current density of 2000 mA g^{-1} , as shown in Fig. 4e. In sharp contrast to the NiCo₂N@C-NCNT nanocomposite, the capacity of NiCo₂O₄-CNTs nanocomposite was $\sim 249.5 \text{ mA h g}^{-1}$ in the 4th cycle at current density of 2000 mA g^{-1} , and it remained at $\sim 217.3 \text{ mA h g}^{-1}$ after 500 cycles (dark yellow and cyan curves for the discharge and charge curves, respectively). These results clearly demonstrate the superiority of NiCo₂N@C-NCNT nanocomposites over oxide counterparts in the anode application of LIBs. Moreover, due to their particular compositions and structures, NiCo₂N@C-NCNT nanocomposites have potential applications in other metal-ion batteries, such as sodium and potassium ion batteries.^{40,41}

To understand the outstanding electrochemical performance of the $\text{NiCo}_2\text{N}@\text{C-NCNT}$ nanocomposites, their structural evolution upon Li^+ insertion and extraction processes was evaluated by *in situ* TEM experiments with a dual-probe biasing TEM sample holder (Fig. S9†).^{42,43} Fig. 5a depicts the as-prepared $\text{NiCo}_2\text{N}@\text{C-NCNT}$ nanocomposites before lithiation. A bias of -3 V was applied to initiate the Li^+ insertion process. After lithiation was initiated for ~ 10 s (Fig. 5b), the Li^+ ions appeared to move rapidly on the surface of NCNTs and then intercalated/reacted with the NiCo_2N nanoparticles. After ~ 10 min, no further variation of the structure of the electrode materials could be detected, indicating reaction completion, as

shown in Fig. 5c. The microstructure of each $\text{NiCo}_2\text{N}@\text{C}$ nanoparticle has evolved from a crystal structure to a particle with numerous nanograins embedded in the Li_xN and carbon matrix during the lithiation process. Fig. 5d shows a HRTEM image of a fully lithiated NiCo_2N nanoparticle, which consists of numerous nanograins with sizes of ~ 2 nm. A few nanograins with a fringe spacing of ~ 0.21 nm indicate the crystalline Co and Ni metals. It reveals that the lithiation reaction of NiCo_2N nanoparticles involves the conversion of the NiCo_2N phase to Co, Ni and Li_xN species. Furthermore, the surfaces and edges of numerous Ni and Co nanograins were coated by a uniform layer of Li_xN with a thickness of $2\text{--}5$ nm. Interestingly, $\text{NiCo}_2\text{N}@\text{C}$

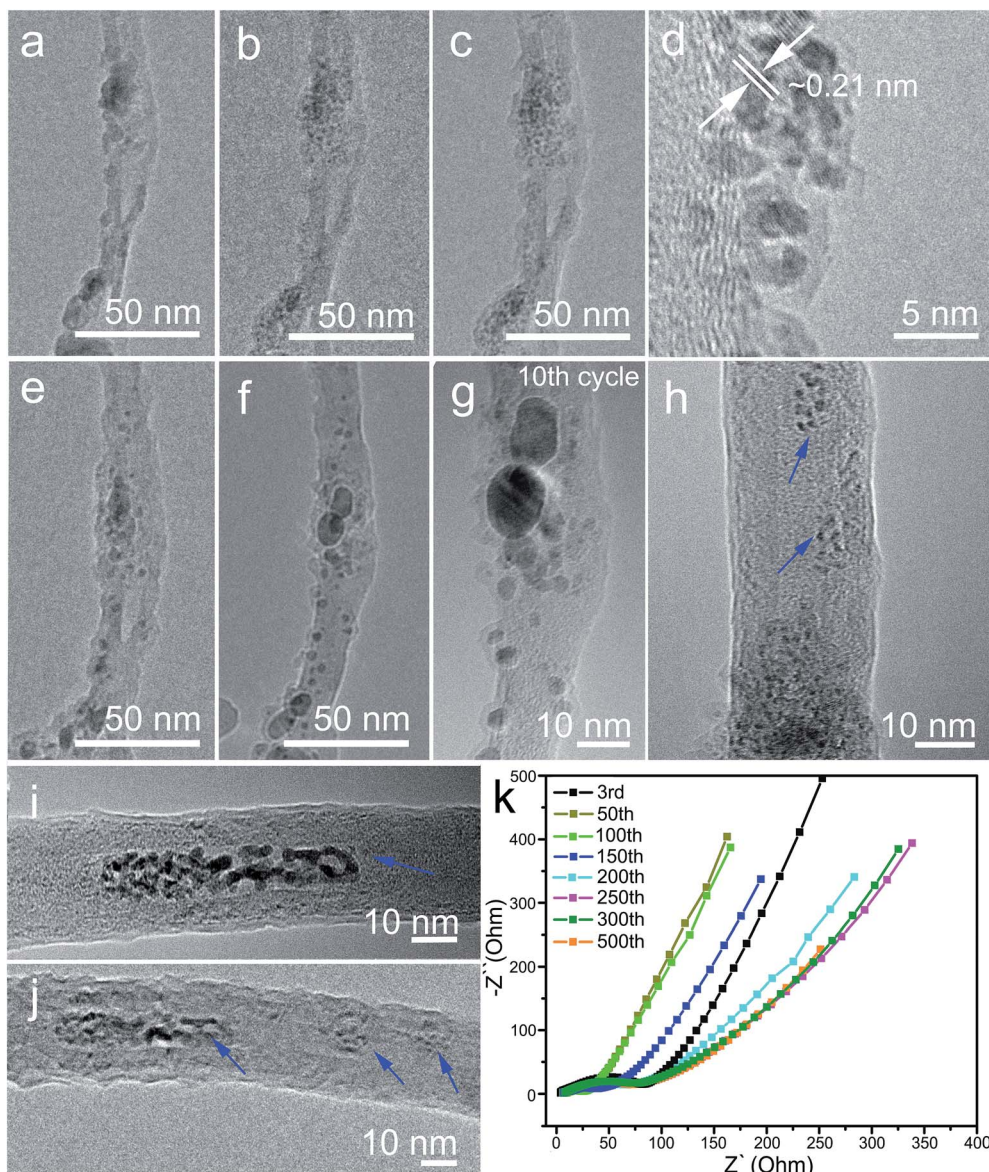


Fig. 5 Structural evolution of the $\text{NiCo}_2\text{N}@\text{C-NCNT}$ nanocomposite during the lithiation and delithiation processes. (a–c) Morphological evolution of the $\text{NiCo}_2\text{N}@\text{C-NCNT}$ nanocomposite during the Li^+ insertion process at 0, 0.5, and 10 min, respectively. (d) HRTEM image of the $\text{NiCo}_2\text{N}@\text{C-NCNT}$ nanocomposite at 10 min after full Li^+ insertion. (e and f) TEM images of the $\text{NiCo}_2\text{N}@\text{C-NCNT}$ nanocomposite after the Li^+ extraction process in the first cycle. (g) TEM image of the $\text{NiCo}_2\text{N}@\text{C-NCNT}$ nanocomposite after the Li^+ extraction process in the 10th cycle. (h and i) TEM images of the $\text{NiCo}_2\text{N}@\text{C-NCNT}$ nanocomposite after the Li^+ extraction during the 10th and 20th cycles. (j) TEM image of the $\text{NiCo}_2\text{N}@\text{C-NCNT}$ nanocomposite after multiple cycles of Li^+ extraction. (k) Nyquist plots of the $\text{NiCo}_2\text{N}@\text{C-NCNT}$ nanocomposite electrode measured with an amplitude of 5 mV over a frequency range from 100 kHz to 0.01 Hz.

nanoparticles on the NCNT showed no isotropic volume expansion during the lithiation process but did show an anisotropic expansion and propagation along the surface of the NCNTs. After completion of the Li^+ insertion, disciform lithiated $\text{NiCo}_2\text{N}@\text{C}$ nanoparticles containing of Co, Ni, C, Li_xC_6 and Li_xN were closely wrapped by NCNTs. The lithiated structure provides highly efficient pathways for the fast electron/ion transfer in the electrodes, which could result in high capacities and improved stability for electrode materials.

After the first full lithiation process, a potential of +3 V was applied to the lithiated $\text{NiCo}_2\text{N}@\text{C}$ -NCNT nanocomposite for the Li^+ extraction process, and the results are shown in Fig. 5e and Fig. 5f is a representative TEM image of the $\text{NiCo}_2\text{N}@\text{C}$ -NCNT nanocomposite after full delithiation. It can clearly be seen that the thin Li_xN layers almost disappeared. The disciform lithiated NiCo_2N nanoparticles shrank in size, but the gross structure of the $\text{NiCo}_2\text{N}@\text{C}$ -NCNT nanocomposites remained unchanged after the delithiation process. Importantly, even after 10 cycles of lithiation and delithiation (Fig. 5g), the structure of the $\text{NiCo}_2\text{N}@\text{C}$ -NCNT nanocomposite had still no distinct change, and thus contributed to the superior cycling performance of the composite. More importantly, the N-doping process generates extrinsic defects in the walls, through which Li^+ ions can diffuse into the interwall space through surface defects or open-ends, thus causing for the formation of pores and even decomposition of CNTs.^{44,45} NiCo_2N nanoparticles on the NCNT surfaces transformed to numerous Ni or Co nanograins embedded in the Li_2O matrix during the lithiation process, and then numerous Ni or Co nanograins moved inside the NCNTs due to the dispersion of extremely small Ni or Co nanograins on the NCNTs throughout by N-doping function.^{46,47} As time passes, partially lithiated NiCo_2N passed the wall of NCNTs into the interwall space, and agglomerated into dark spots inside the NCNTs, as shown in Fig. 5h. As a result, more nanograins moved inside the NCNTs (Fig. 5g). Such NiCo_2N nanoparticles inside the NCNT structure could serve as defensive tools for MN nanoparticles to help protect themselves during the lithiation/delithiation process, which confines the volume change, prevents inner nanoparticles from reacting with the electrolyte, limits the amount of the SEI layer and better utilization of active materials and the electrolyte, ensures a more direct electrical path and guarantees a large capacity and long stability at different current densities. Besides, the relatively large volumetric expansion (<10%) of NCNTs with filled nanoparticles during the lithiation process (Fig. 5j) was confirmed in comparison with NCNTs without filled nanoparticles (Fig. 5h). The volumetric expansion of NCNTs is attributed to the swollen NiCo_2N nanoparticles after lithiation which occupy the entire NCNT's hollow space, which could transform the pristine stable structures, increase resistance of electrodes and decrease the specific capacity (after ~200 cycles in Fig. 4e). Finally, both positive and negative effects from morphological variation of NiCo_2N nanoparticles and NCNTs would reach an equilibrium state, which results in a stable electrochemical performance during the lithiation/delithiation process. To further elucidate the structures of NiCo_2N inside NCNTs, EDX elemental mapping was applied to

characterize the $\text{NiCo}_2\text{N}@\text{NCNT}$ nanocomposites after 500 cycles. As shown in Fig. S10,[†] Co, Ni and N elements are well-dispersed inside the NCNTs and overlapped with each other, which shows the successful movement of nanograins to the inner space of NCNTs. Therefore, a variation mechanism of the $\text{NiCo}_2\text{N}@\text{C}$ -NCNT nanocomposite during cycling was discovered by *in situ* TEM.

The correlation between *ex situ* electrochemical impedance spectra (EIS) and *ex situ* morphology of the $\text{NiCo}_2\text{N}@\text{C}$ -NCNT nanocomposite electrodes was also studied. The EIS of the $\text{NiCo}_2\text{N}@\text{C}$ -NCNT nanocomposite electrodes at a current density of 200 mA g^{-1} were collected for the characterization of the resistance change during the lithiation and delithiation processes,^{48,49} as shown in Fig. 5k. For the $\text{NiCo}_2\text{N}@\text{C}$ -NCNT nanocomposite electrode, resistance for the electron transport has increased from the 3rd to 50th, decreased from 50th to 250th, and then gradually becomes stable after 250 cycles. The enhanced electrical conductivities of the $\text{NiCo}_2\text{N}@\text{C}$ -NCNT nanocomposite electrode from 3rd to 50th cycles were as a result of the initial activation of the $\text{NiCo}_2\text{N}@\text{C}$ -NCNT nanocomposites and 'self-protection' of part of the active materials inside the NCNTs, in accordance with the steadily improved cycling performance. The characteristic of the $\text{NiCo}_2\text{N}@\text{C}$ -NCNT nanocomposite electrode after 500 cycles at a high current density of 2000 mA g^{-1} was also examined by SEM (Fig. S11[†]) and TEM (Fig. S12[†]). It is discernible that the electrode of the $\text{NiCo}_2\text{N}@\text{C}$ -NCNT nanocomposite could still retain its structural integrity even after the 150th cycle (Fig. S11a[†]) except for the increased roughness on the electrode surface, which indicates that the insertion and extraction of the lithium ion have no distinct impact on the composite structure due to sufficient free space for the expansion of filled NiCo_2N nanoparticles inside the void structure of the cross-linked NCNTs in the $\text{NiCo}_2\text{N}@\text{C}$ -NCNTs nanocomposite electrode. The electrode composed of the $\text{NiCo}_2\text{N}@\text{C}$ -NCNTs nanocomposite could be observed slight fissure after 250 cycle (Fig. S11b[†]), and the amount of fissure has no obvious increase after 500 cycles (Fig. S11c[†]). The result suggested the relatively balanced effects between volumetric expansion and 'self-protection' of active materials inside NCNTs after cycles. Moreover, the nanostructures of the $\text{NiCo}_2\text{N}@\text{C}$ -NCNT nanocomposite illustrated by TEM still sustain their structural integrity after 250 and 500 cycles, except for the increased roughness on the surface and diameter of the NCNTs (~8%). These *ex situ* measurements are corresponded to the results for $\text{NiCo}_2\text{N}@\text{C}$ -NCNT nanocomposites during the cycle process from *in situ* TEM observations. The structural evolution and 'self-protection' mechanism during lithiation/delithiation afford the prerequisite for obtaining an enlarged capacity during initial cycles, change in the specific value, and reaching a steady state during the subsequent cycles.

Conclusions

In summary, the synthesis of $\text{NiCo}_2\text{N}@\text{C}$ -NCNT nanocomposites by a facile method and their anode application in LIBs were reported for the first time. This work reveals that the



NiCo₂N electrode materials have more Li⁺ channels and higher electrical conductivity compared to the NiCo₂O₄ electrode materials. *In situ* TEM observations verify that some of the NiCo₂N nanoparticles spread along the surface of NCNTs, and enter the NCNTs to 'protect themselves', which delivers the excellent cycling stability of the composite electrodes. Besides, NiCo₂N@C-NCNT nanocomposites provide good electron and ion-transport capability and sufficient void space by cross-linked NCNTs during cycling. The NiCo₂N@C-NCNT nanocomposite electrodes exhibited outstanding lithium-storage performance including high specific capacity, excellent cycling stability and remarkable rate performance. A reversible capacity of ~624.5 mA h g⁻¹ was obtained at a current density of 2000 mA g⁻¹, and retained ~569.1 mA h g⁻¹ after 500 cycles (retention close to 104.2% after 500 cycles). The notable overall properties of the NiCo₂N@C-NCNT nanocomposite approach make it a promising anode material candidate for high-performance LIBs.

Conflicts of interest

The authors declare no conflict of interest.

Acknowledgements

This work was financially supported by the National Natural Science Foundation of China (grant no. 51472049, 51741203 and 51672044), the Shanghai Pujiang Program (grant no. 16PJ1400200), the Science and Technology Commission of Shanghai Municipality (18ZR1402000), the Program for Innovative Research Team in University of Ministry of Education of China (IRT_16R13), the DHU Distinguished Young Professor Program and the Fundamental Research Funds for the Central Universities and Engineering and Physical Sciences Research Council (EP/L015862/1, EP/N032888/1, EP/K002252/1, EP/L018330/1 and EP/K021192/1). The author would also like to acknowledge the use of the UCL Grace High performance computing facility (Grace@UCL) and associated support services, in completing this work.

References

- 1 M. T. McDowell, S. W. Lee, W. D. Nix and Y. Cui, *Adv. Mater.*, 2013, **25**, 4966.
- 2 P. Albertus, S. Babinec, S. Litzelman and A. Newman, *Nat. Energy*, 2018, **3**, 16.
- 3 W. Long, B. Fang, A. Ignaszak, Z. Wu, Y. J. Wang and D. Wilkinson, *Chem. Soc. Rev.*, 2017, **46**, 7176.
- 4 N. Liu, Z. Lu, J. Zhao, M. T. McDowell, H.-W. Lee, W. Zhao and Y. Cui, *Nat. Nanotechnol.*, 2014, **9**, 187.
- 5 Q. Liu, Z. Cui, R. Zou, J. Zhang, K. Xu and J. Hu, *Small*, 2017, **13**, 1603754.
- 6 Y. M. Chen, X. Y. Yu, Z. Li, U. Paik and X. W. Lou, *Sci. Adv.*, 2016, **2**, e1600021.
- 7 W. C. Chang, K. W. Tseng and H. Y. Tuan, *Nano Lett.*, 2017, **17**, 1240.
- 8 R. J. Zou, Z. Z. Zhang, M. F. Yuen, M. L. Sun, J. Q. Hu, C. S. Lee and W. J. Zhang, *NPG Asia Mater.*, 2015, **7**, e195.
- 9 Y. Zhao, J. Feng, X. Liu, F. Wang, L. Wang, C. Shi, L. Huang, X. Feng, X. Chen, L. Xu, M. Yan, Q. Zhang, X. Bai, H. Wu and L. Mai, *Nat. Commun.*, 2014, **5**, 4565.
- 10 M. Ko, S. Chae, J. Ma, N. Kim, H.-W. Lee, Y. Cui and J. Cho, *Nat. Energy*, 2016, **1**, 16113.
- 11 Y. Wang, L. Yu and X. W. Lou, *Angew. Chem., Int. Ed.*, 2016, **55**, 14668.
- 12 Y. Shi, J. Zhang, A. M. Bruck, Y. Zhang, J. Li, E. A. Stach, K. J. Takeuchi, A. C. Marschilok, E. S. Takeuchi and G. Yu, *Adv. Mater.*, 2017, **29**, 1603922.
- 13 G. Chen, L. Yan, H. Luo and S. Guo, *Adv. Mater.*, 2016, **28**, 7580.
- 14 L. Zhou, Z. Zhuang, H. Zhao, M. Lin, D. Zhao and L. Mai, *Adv. Mater.*, 2017, **29**, 1602914.
- 15 M.-S. Balogun, Y. Huang, W. Qiu, H. Yang, H. Ji and Y. Tong, *Mater. Today*, 2017, **20**, 425.
- 16 Y. Zhang, B. Ouyang, J. Xu, G. Jia, S. Chen, R. S. Rawat and H. J. Fan, *Angew. Chem., Int. Ed.*, 2016, **55**, 8670.
- 17 M.-S. Balogun, M. Yu, Y. Huang, C. Li, P. Fang, Y. Liu, X. Lu and Y. Tong, *Nano Energy*, 2015, **11**, 348.
- 18 H. Xu, H. Zhang, L. Fang, J. Yang, K. Wu and Y. Wang, *ACS Nano*, 2015, **9**, 6817.
- 19 Y. Dong, B. Wang, K. Zhao, Y. Yu, X. Wang, L. Mai and S. Jin, *Nano Lett.*, 2017, **17**, 5740.
- 20 M. S. Balogun, M. Yu, C. Li, T. Zhai, Y. Liu, X. Lu and Y. Tong, *J. Mater. Chem. A*, 2014, **2**, 10825.
- 21 L. Han, K. Feng and Z. Chen, *Energy Technol.*, 2017, **5**, 1908.
- 22 Y. Wang, B. Zhang, W. Pan, H. Ma and J. Zhang, *ChemSusChem*, 2017, **10**, 4170.
- 23 G. Kresse and J. Furthmüller, *Comput. Mater. Sci.*, 1996, **6**, 15.
- 24 J. Hubbard, *Proc. R. Soc. London, Ser. A*, 1963, **276**, 238.
- 25 J. P. Perdew, K. Burke and M. Ernzerhof, *Phys. Rev. Lett.*, 1996, **77**, 3865.
- 26 P. E. Blöchl, *Phys. Rev. B: Condens. Matter Mater. Phys.*, 1994, **50**, 17953.
- 27 G. Kresse and D. Joubert, *Phys. Rev. B: Condens. Matter Mater. Phys.*, 1999, **59**, 1758.
- 28 L. Wang, T. Maxisch and G. Ceder, *Phys. Rev. B: Condens. Matter Mater. Phys.*, 2006, **73**, 195107.
- 29 G. Henkelman, B. P. Uberuaga and H. Jónsson, *J. Chem. Phys.*, 2000, **113**, 9901.
- 30 G. Henkelman and H. Jónsson, *J. Chem. Phys.*, 2000, **113**, 9978.
- 31 J. Hou, C. Cao, F. Idrees and X. Ma, *ACS Nano*, 2015, **9**, 2556.
- 32 Y. Yu, W. Gao, Z. Shen, Q. Zheng, H. Wu, X. Wang, W. Song and K. Ding, *J. Mater. Chem. A*, 2015, **3**, 16633.
- 33 S. Dou, L. Tao, J. Huo, S. Wang and L. Dai, *Energy Environ. Sci.*, 2016, **9**, 1320.
- 34 C. Hu and L. Dai, *Adv. Mater.*, 2017, **29**, 1604942.
- 35 G. Gao, H. B. Wu and X. W. Lou, *Adv. Energy Mater.*, 2014, **4**, 1400422.
- 36 L. Shen, L. Yu, X.-Y. Yu, X. Zhang and X. W. Lou, *Angew. Chem., Int. Ed.*, 2015, **54**, 1868.
- 37 L. Zhang, L. Zuo, W. Fan and T. Liu, *ChemElectroChem*, 2016, **3**, 1384.
- 38 H. C. Gao, W. D. Zhou, K. Park and J. B. Goodenough, *Adv. Energy Mater.*, 2016, **6**, 1600467.



39 H. C. Gao and J. B. Goodenough, *Angew. Chem., Int. Ed.*, 2016, **55**, 12768.

40 H. C. Gao, L. G. Xue, S. Xin and J. B. Goodenough, *Angew. Chem., Int. Ed.*, 2018, **57**, 5449.

41 H. C. Gao, L. G. Xue, S. Xin, K. Park and J. B. Goodenough, *Angew. Chem., Int. Ed.*, 2017, **56**, 5541.

42 X. H. Liu, Y. Liu, A. Kushima, S. Zhang, T. Zhu, J. Li and J. Y. Huang, *Adv. Energy Mater.*, 2012, **2**, 722.

43 R. Zou, Z. Cui, Q. Liu, G. Guan, W. Zhang, G. He, J. Yang and J. Hu, *J. Mater. Chem. A*, 2017, **5**, 20072.

44 X. H. Liu, J. W. Wang, Y. Liu, H. Zheng, A. Kushima, S. Huang, T. Zhu, S. X. Mao, J. Li, S. Zhang, W. Lu, J. M. Tour and J. Y. Huang, *Carbon*, 2012, **50**, 3836.

45 L. G. Bulusheva, A. V. Okotrub, A. G. Kurenya, H. K. Zhang, H. J. Zhang, X. H. Chen and H. H. Song, *Carbon*, 2011, **49**, 4013.

46 G. Melinte, S. Moldovan, C. Hirlimann, X. Liu, S. Bégin-Colin, D. Bégin, F. Banhart, C. Pham-Huu and O. Ersen, *Nat. Commun.*, 2015, **6**, 8071.

47 W. H. Shin, H. M. Jeong, B. G. Kim, J. K. Kang and J. W. Choi, *Nano Lett.*, 2012, **12**, 2283.

48 H. Jiang, Y. Hu, S. Guo, C. Yan, P. S. Lee and C. Li, *ACS Nano*, 2014, **8**, 6038.

49 L. Wang, L. Zhuo, H. Cheng, C. Zhang and F. Zhao, *J. Power Sources*, 2015, **283**, 289.